

High-resolution Rayleigh imaging of dissipative structures in a turbulent jet flame

Jonathan H. Frank, Sebastian A. Kaiser

Combustion Research Facility
Sandia National Laboratories
Livermore, CA 94551, USA
jhfrank@ca.sandia.gov

Abstract High-resolution laser Rayleigh imaging is used to measure the detailed structure of the thermal dissipation field in a turbulent non-premixed $\text{CH}_4/\text{H}_2/\text{N}_2$ jet flame with a jet-exit Reynolds number of 15,200. Measurements are performed in the near field ($x/d = 5-20$) of the jet flame where the primary combustion reactions interact with the turbulent flow. The dissipation field exhibits thin layers of high dissipation, and the layer thicknesses are measured as a function of temperature and downstream position. Adaptive smoothing suppresses noise in the temperature-gradient measurements and enables accurate determination of the dissipation-layer widths from single-shot measurements. Probability density functions (PDF) of the dissipation layer widths conditioned on temperature are approximately log-normal distributions. The conditional PDFs at each downstream location approximately scale with temperature to the 0.75 power. The contributions of both the axial and radial gradients to the thermal dissipation are determined from the two-dimensional dissipation measurements. The relative contributions of the two components varies significantly with radial position. Near the jet centerline, the axial and radial contributions are comparable. Away from the jet centerline, the combined effects of flow shear between the jet and the surrounding coflow and flow laminarization due to the flame heat release induce a preferred orientation of the dissipation layers that results in significantly larger dissipation in the radial direction. The high signal-to-noise ratios of the Rayleigh images coupled with an interlacing technique for noise suppression enable measurements of the mean power spectral density (PSD) of the temperature gradients with a dynamic range of three orders of magnitude. These fully resolved power spectra are used to determine the turbulent microscales by measuring a cutoff wavelength, λ_c , at 2% of the peak PSD. This cutoff criterion is based on models of 1-D power spectra for non-reacting turbulent flows. The Batchelor scale is estimated from λ_c , and the results are compared with Batchelor scales estimated from scaling laws in non-reacting flows using the local Reynolds number. At $x/d = 20$, the different approaches to determining the Batchelor scale are comparable. Closer to the nozzle, there is a discrepancy between the two methods.

1. Introduction

In turbulent nonpremixed flames, the scalar dissipation rate, χ , is a fundamental quantity that governs the rate of molecular mixing and the reaction rate. The scalar dissipation rate is given by $\chi = 2D(\nabla\xi \cdot \nabla\xi)$, where D is the mass diffusivity and ξ is the mixture fraction. The measurement of scalar dissipation in flames is extremely challenging because it requires evaluating the gradient of mixture fraction over a wide range of length scales. This requires multi-dimensional mixture fraction measurements with large signal-to-noise ratios (SNR). Scalar dissipation measurements in flames have been performed using both two-dimensional (Frank 1994, 2002, 2005, Fielding 1998, Kelman 1994, Stärner 1994, Long 1993) and one-dimensional (Karpetis 2002, 2005, Geyer 2004) multi-scalar imaging. The optimization of diagnostic techniques for measuring mixture fraction gradients is an ongoing research area, and significant progress has been made in recent years. One of the primary challenges is the modest SNRs and spatial resolutions in the detection of relatively weak scattering processes, such as Raman scattering or two-photon laser-induced fluorescence (LIF).

In this study, we consider a complementary high-resolution and high-SNR measurement that probes the dissipative structures in the temperature field using only laser Rayleigh scattering. The dissipative structures in the temperature field are characterized by the thermal dissipation, $\chi_T = 2\alpha(\nabla T' \cdot \nabla T')$, which depends on both the gradient of the temperature fluctuation, $T' = T - \langle T \rangle$, and the local thermal diffusivity α . The thermal diffusivity approximately scales with temperature as $\alpha \propto T^{1.72}$ (Wang et al. 2005a) and varies by a factor of ~ 27 over the temperature range in the flame considered here. As a result, measurements of χ_T at high temperatures are significantly more sensitive to noise than are measurements of the gradient-squared term, $|\nabla T'|^2 = \nabla T' \cdot \nabla T'$. In the present study, we focus on the $|\nabla T'|^2$ term because it contains the significant structural detail of the dissipation field and is less sensitive to noise than χ_T .

Previous thermal dissipation measurements include high-repetition rate point measurements in the far field of jet flames (Wang et al. 2005b). In those studies, thermal dissipation length scales were inferred from time series temperature measurements using Taylor's hypothesis. To date, the application of this approach in jet flames has been limited to the measurement of dissipative scales in the far field, where the spatial scales are relatively large and commercially available lasers provide sufficiently high repetition rates to resolve the length scales. We have demonstrated an alternative approach that resolves dissipation scales in the near field of jet flames, where the primary combustion reactions occur (Kaiser 2006). This approach uses 2-D imaging to directly measure the thermal dissipation structures, and hundreds of images are acquired to determine ensemble statistics of the dissipative scales in both the axial and radial coordinates of jet flames. A concurrent experimental study uses line imaging of Rayleigh scattering to provide 1-D thermal dissipation measurements along the radial coordinate of jet flames (Wang et al. 2006).

The present study focuses on the near field of jet flames because it is particularly important for understanding turbulence-flame interactions and is a challenging location for determining scaling laws for turbulent length scales. In the far field of jet flames, the application of traditional scaling laws from the self-similar far field of non-reacting jets may be plausible. The far field is dominated by mixing between the combustion products and the surrounding flow field. However, the combustion reactions occur predominantly in the near field and transitional regions of the jet flame, and these regions have a complex array of length scales with unknown scaling laws. The study of the near field and transitional regions of jet flames is critical for developing accurate models of turbulent non-premixed combustion. In this paper, results from a series of 2-D measurements of the thermal dissipation structures are presented at three downstream locations and a range of radial locations. We consider the evaluation of turbulent length scales of the dissipation structures using both spectral and spatial analyses.

2. Experiment

The experiment was performed in the Advanced Imaging Laboratory at Sandia National Laboratories. The non-premixed turbulent jet flame considered here corresponds to "Flame DLR-A" from the set of target flames in the TNF Workshop (Barlow 2006, Meier et al. 2000). The fuel was a mixture of 22.1% CH₄, 33.2% H₂, and 44.7% N₂ (by volume) with the air of the coflow as the oxidizer. This combination of fuel and oxidizer yields a Rayleigh cross-section that is constant within $\pm 3\%$ throughout the flame (Bergmann et al. 1998), therefore allowing for direct temperature measurements from Rayleigh scattering. The fuel jet issued from a tube with a diameter of $d = 8.0$ mm at an exit Reynolds number of $Re_d = 15,200$ into the filtered air of the coflow.

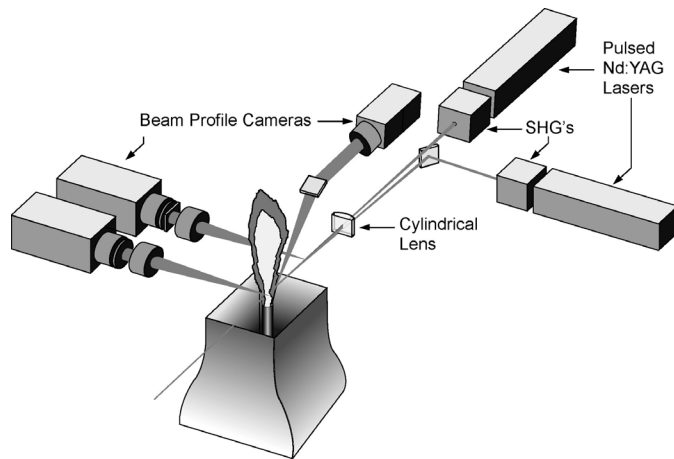


Fig. 1: Experimental arrangement for high-resolution Rayleigh imaging.

The Rayleigh imaging experiment is shown in Fig. 1. The experimental arrangement and data reduction as well as noise and spatial resolution of the resulting images are described in more detail by Kaiser and Frank (2006). A brief summary follows.

The beams of two frequency-doubled Nd:YAG lasers at 532 nm were combined and formed into a sheet with a total energy of 1.8 J/pulse. Rayleigh scattering from the probe volume was imaged onto an unintensified interline-transfer camera by an optimized combination of commercial camera lenses. Additional cameras were used to record shot-by-shot vertical laser intensity profiles and time-averaged horizontal beam overlap and sheet thickness.

Data reduction consisted of corrections for average throughput of the imaging system as well as shot-to-shot beam-profile corrections. Background signal from elastic scattering was negligible. The temperature field was determined from the corrected Rayleigh signal, which is directly proportional to the gas number density. The Rayleigh scattering from room temperature air was used as a reference signal.

The projected pixel area of the Rayleigh images was $20.7 \times 20.7 \mu\text{m}^2$. A more complete characterization of the resolution is given by the line spread function (LSF) of the imaging system which was measured using a scanning-edge technique (Wang and Clemens 2004). The full width at half maximum of the LSF was 24 μm in the center of the image, which is equivalent to a standard deviation σ_{LSF} of 10.2 μm . Potential degradation of this native resolution due to noise-suppressing filters will be discussed below. The average $1/e^2$ full width laser sheet thickness was 150 μm , or equivalently, the standard deviation σ_{sheet} of the profile was 38 μm , which was a factor of 3.7 coarser than the in-plane resolution. However, preliminary analysis indicates that the effect of out-of-plane averaging on the gradients calculated by in-plane differentiation is minor for the measurements presented here. In the analysis that follows, we neglect the influence of the finite sheet thickness.

3. Results and Discussion

The length scales of thermal dissipation structures are investigated at three downstream locations in the near field of the jet flame. At each downstream location, measurement positions were tiled as necessary to radially span the half-width of the flow. Except where noted, in each image a region of 688×256 pixels (14.4 mm x 5.3 mm) width x height was evaluated. Figure 2

shows an example of high-resolution measurements of the squared gradient of the temperature fluctuation, $|\nabla T'|^2 = (\partial T'/\partial x)^2 + (\partial T'/\partial r)^2$, at $x/d = 5, 10$, and 20 . Gaussian smoothing with a temperature-dependent kernel size has been applied to the temperature field before differentiation. The details of this adaptive smoothing technique will be discussed in Section 3.2. The intricate structures of the lower temperature region near the jet centerline are resolved in detail, and the effects of heat release are evident from the change in the structures in the higher temperature regions.

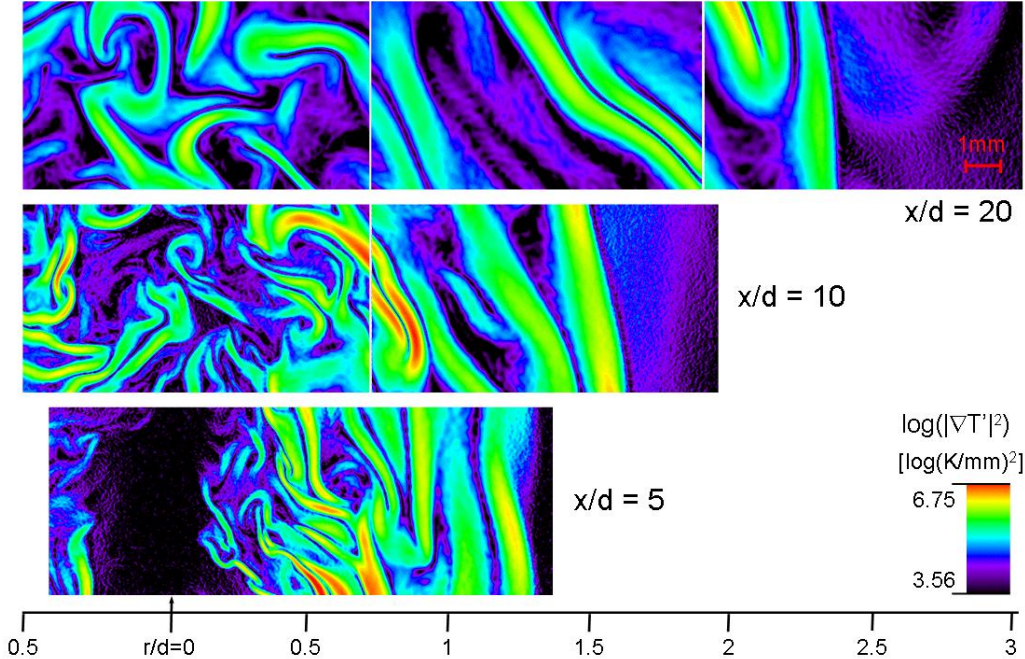


Fig. 2: Single-shot measurements of the gradient-square of the temperature fluctuation, $|\nabla T'|^2$, at the three downstream locations. The images spanning the field radially are acquired separately and have been cropped to provide continuous radial coverage.

A series of 600 images were used to compile statistics of thermal dissipation at these three downstream locations. The top row of Fig. 3 shows the radial profiles of the mean and root-mean-squared (rms) temperature. The mean temperatures on the jet axis are 294 K, 414 K, and 860 K at $x/d = 5, 10$, and 20 , respectively. The peak mean temperatures are between 1556 K and 1665 K with instantaneous temperatures reaching 2050 K. The bottom row of Fig. 3 shows mean radial profiles of $|\nabla T'|^2$, as well as the radial and axial contributions to $|\nabla T'|^2$. These profiles were calculated using interlacing to eliminate noise bias from the mean values of $|\nabla T'|^2$. The details of this noise suppression technique will be discussed in Section 3.1. The radial and axial contributions are approximately equal on the jet centerline, where the turbulence is relatively isotropic and there is not a strongly preferred orientation of the dissipation structures. The radial contribution peaks at a larger radial location than the axial component. At $x/d = 5$ and 10 , the peak location of the total dissipation occurs near the peak of the axial component. At $x/d = 20$, the radial decay of the axial component is offset by the increase in the radial component, and the total dissipation profile has a broad plateau for $0.5 < r/d < 2.5$. As the radial location increases from the jet centerline, the combined effects of flow shear between the jet and the coflow and flow laminarization due to the flame heat release induce a preferred orientation of the dissipation layers that results in larger dissipation in the radial direction. The variation of angular distribution of the dissipation structures

is evident in the images of Fig. 2. At the radial location of peak mean temperature in Fig. 3, the radial contribution is the dominant contribution to the dissipation. At larger radial locations, the dissipation is almost entirely the result of the radial contribution. The differences between the axial and radial contributions to the dissipation indicate the need for multi-dimensional dissipation measurements to fully capture the structure of the dissipation field.

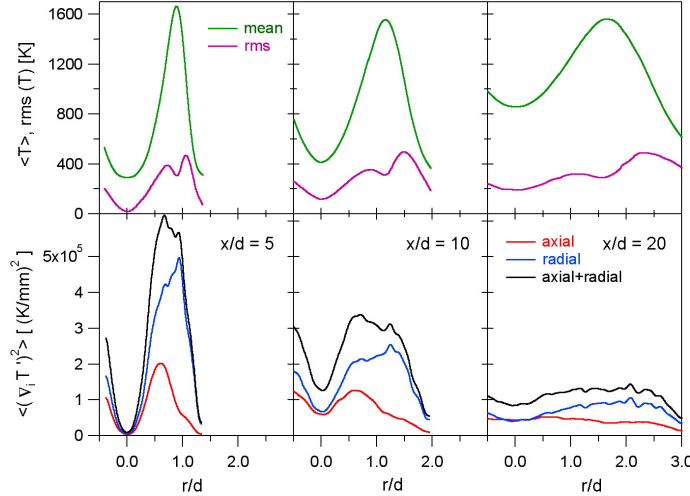


Fig. 3: Radial profiles of mean and rms temperature at three downstream locations (top row).

Mean radial profiles of $|\nabla T'|^2$, $(\partial T'/\partial x)^2$, and $(\partial T'/\partial r)^2$ (bottom row).

3.1 Spectral Analysis of Thermal Dissipation Structures

Spectral analysis of the temperature gradients provides insight into the distribution of length scales in the thermal dissipation field. The high signal-to-noise ratios of the Rayleigh images coupled with a noise suppression technique provides fully resolved measurements of the mean power spectral density (*PSD*) of the temperature gradients. In evaluating the power density spectra, we use an interlacing technique to significantly reduce the noise. Figure 4 shows a sample power spectral density for the radial component of the temperature gradient, $PSD = |FFT_r(\partial T'/\partial r)|^2$, where FFT_r indicates the forward Fast Fourier Transform in the radial direction. The spectrum is computed from 600 shots using a 20.7- μm pixel spacing in a 256 x 256 pixel ($5.3 \times 5.3 \text{ mm}^2$) region centered at $x/d = 10$ and $r/d = 1$. The *PSD* evaluated without interlacing exhibits a monotonic decay with increasing spatial frequency for frequencies less than 2 mm^{-1} . For larger spatial frequencies, noise becomes dominant, and the *PSD* increases. The resulting spectrum has a limited dynamic range of approximately 40. In the interlacing approach, each temperature image is separated into two fields by sampling alternate rows of pixels. To the extent that the noise in neighboring rows of pixels is uncorrelated, the noise contribution to the mean spectrum cancels. The resulting interlaced power spectral density is given by $PSD_r^{\text{IL}} = |FFT_r(\partial T_1'/\partial r)FFT_r^*(\partial T_2'/\partial r)|$, where T_1' and T_2' are the temperature fluctuations from the odd and even fields, respectively, and FFT_r^* indicates the complex conjugate of the Fast Fourier Transform. In Fig. 4, the *PSD* with interlacing shows a significant reduction of the noise and indicates that the interlaced spectrum is resolved over three orders of magnitude. Noise becomes significant at frequencies greater than 3.5 mm^{-1} , but does not rise with increasing frequencies. The interlacing technique is also applicable to the evaluation of the mean squared temperature gradient. Figure 4 also shows the *PSD* after images are filtered by Gaussian

smoothing with a kernel size that varies as a function of local temperature. Details of the smoothing algorithm will be discussed in Section 3.2.

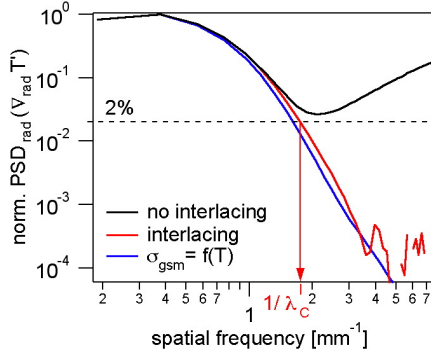


Fig. 4: Power spectral density of the radial gradient of the temperature fluctuation with and without interlacing. The spectra are normalized by the mean gradient-square $\langle |\nabla T|^2 \rangle$.

The ability to resolve the power spectrum over three orders of magnitude enables us to estimate the turbulent microscales in the thermal dissipation field using an analysis similar to the well-established methods in studies of non-reacting flows. On the basis of Pope's (2000) 1-D model spectrum for non-reacting flows, Wang et al. (2006) estimate that the spatial frequency corresponding to 2% of the peak power spectral density is a cutoff frequency above which there is less than 1% contribution to the mean dissipation. We denote the corresponding cutoff wavelength as λ_C , as illustrated in Fig. 4. In non-reacting flows, the turbulent microscales can be estimated from λ_C . The Batchelor scale, λ_B , is proportional to λ_C with $\lambda_B = \lambda_C / 2\pi$, and the Kolmogorov scale, η_K , is given by $\lambda_B = \eta_K Sc^{-1/2}$, where Sc is the Schmidt number. In gas phase flows, Schmidt numbers are near unity, and $\lambda_B \approx \eta_K$.

We estimate λ_B as a function of radial position at $x/d = 5, 10$, and 20 by determining λ_C from the 2% of the peak $PSDs$ for subregions at different radial positions. At $x/d = 5$, the width of the evaluated region was 128 pixels (2.7 mm), at $x/d = 10$ and 20 a region of 256 pixels (5.3 mm) width was used. Figure 5 displays a series of peak-normalized $PSDs$ for the radial temperature gradients. At each downstream location, the progression of the $PSDs$ illustrates the growth in turbulent length scales with increasing radial position. Table 1 compares the values of $\lambda_C/2\pi$ using the $PSDs$ in Fig. 5 with estimates of the Batchelor scale based on scaling laws for non-reacting jet flows. From scaling laws in non-reacting jet flows, the Batchelor scale can be estimated from the local Reynolds number, Re_δ , by

$$\lambda_B = 2.3\delta Re_\delta^{-3/4} Sc^{-1/2} \quad (2)$$

(Wang et al 2005a,b and references therein), where δ is the full width at half maximum of the measured velocity profiles (Schneider et al 2003), and $Re_\delta = U_{CL}\delta/\nu_{CL}$, where U_{CL} and ν_{CL} are the centerline velocities and kinematic viscosities, respectively. The mixture averaged kinematic viscosities are calculated using transport properties from GRI-Mech 3.0[ref.] and centerline compositions and temperatures from the point measurements compiled in the TNF database (Barlow 2006). The scaling law in Eq. 2 is not necessarily applicable to the developing turbulence in the near field of a jet flow, and the addition of heat release from combustion further complicates the estimation of the relevant turbulent microscales. However, it is instructive to compare microscale estimates from this scaling law with measurements of λ_C . A comparison of the

values in Table 1 shows that the nonreactive scaling law estimates give an order of magnitude estimate of the microscales at the jet centerline. At $x/d = 20$, the non-reacting flow estimates agree well with the values determined from the spectral cutoff wavelengths. The agreement degrades at $x/d = 5$ and 10.

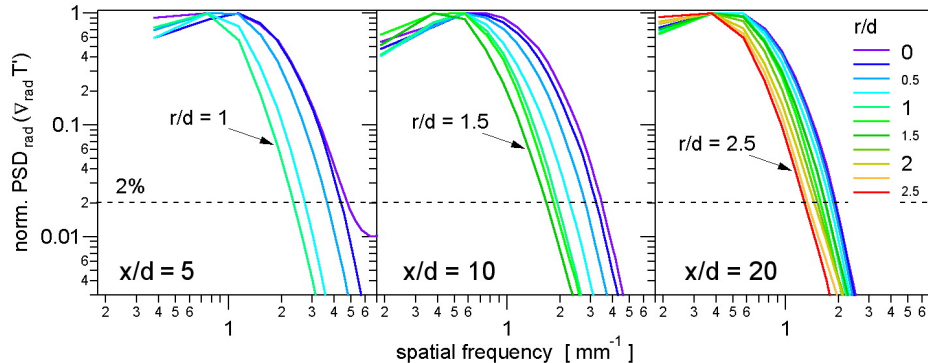


Fig. 5: Interlaced radial power density spectra of the temperature fluctuation gradient for three axial locations ($x/d = 5, 10, 20$) and radial position spanning the flame.

x/d	λ_B	$\lambda_C/2\pi$
5	10 μm	38-67 μm
10	25 μm	48-95 μm
20	75 μm	81-123 μm

Table 1: Comparison of turbulent microscales determined from the local Reynolds number using Eq. 2, and from the 2% cutoff of the PSD . Values of $\lambda_C/2\pi$ are given for the range of radial locations in Fig. 5.

3.2 Spatial Analysis of Thermal Dissipation Structures

Two-dimensional imaging measurements enable us to identify the layered structures in the dissipation field and to determine the thicknesses of these structures. This spatial analysis is complementary to the spectral analysis described above. The thickness of each layer, λ_D , is determined along the direction normal to the layer, which provides a more direct measure of the structure length scales than is possible with 1-D measurements. In 1-D measurements, the layers are measured as projections along the measurement axis, and the interpretation of the structure thickness is complicated by the varying orientations of the layers. A full 3-D measurement is required to completely eliminate this issue. However, the 2-D imaging provides a significant improvement over 1-D measurements.

We investigate the thickness of the layered dissipation structures as a function of temperature as well as downstream and radial positions. The layer thicknesses are measured from the single-shot images of the squared temperature gradient. In order to accurately identify the layers and determine their thicknesses, the noise must be suppressed on a single-shot basis. While the interlacing technique described in Section 3.1 provides excellent noise suppression for the mean power spectra and the mean gradient-square, the suppression is insufficient for evaluating structures in single-shot images. For the layer-width measurements, the temperature images are smoothed to reduce the noise. Smoothing is equivalent to applying a low-pass filter, and there is an inherent tradeoff between the suppression of noise and the reduction of spatial resolution (Mi and Nathan

2003). Homogeneous smoothing with a single smoothing kernel is commonly used but is not optimal for images containing a wide range of length scales. It can lead to unnecessary attenuation of the smallest length scales or inadequate noise suppression for the largest length scales. The temperature dissipation structures are thin layers that span a wide range of length scales, and the larger length scales are associated with the high temperature regions, which have the lowest SNR. We use inhomogeneous smoothing with an isotropic Gaussian kernel whose size (as characterized by the standard deviation σ_{gsm}) is calculated as a function of the local temperature, T . The chosen temperature-dependence is

$$\sigma_{gsm} = \sigma_{gsm,0} \left(\frac{T}{T_0} \right)^\alpha, \quad (1)$$

where T_0 is a reference temperature and $\sigma_{gsm,0}$ is the corresponding reference kernel size. From an initial analysis using homogenous smoothing, we chose $\sigma_{gsm,0} = 0.96, 1.12$, and 1.36 pixels for the images at $x/d = 5, 10$, and 20 , respectively. The reference temperature was 300 K, and the scaling exponent was $\alpha = 0.75$. The resulting kernel sizes varied from approximately 1 to 6 pixels (20 to 120 μm) over the measured range of temperatures.

The effect of this adaptive smoothing on the power spectral density is displayed in Fig. 4. A comparison of the interlaced *PSD* with the *PSD* obtained after temperature-dependent smoothing and without interlacing shows that the smoothing introduces some attenuation of the power spectrum. This attenuation is most noticeable at the highest spatial frequencies. We will assess the impact of this filtering scheme on the layer-width measurements *a posteriori* and will show that good estimates of the local structure size are obtained.

We measure the dissipative layer thicknesses as the full width at 20% of the local maxima of $|\nabla T'|^2$. This approach is adopted for consistency with similar studies in non-reacting flows (Buch and Dahm 1988, Su and Clemens 1999, 2003, Tsurikov and Clemens 2002) and the previous study of Kaiser and Frank (2006). To determine the layer widths, we use a modified version of the procedure of Su and Clemens (2003). This procedure consists of three basic steps:

1. Find the centerlines of the $|\nabla T'|^2$ -layers (the loci of maxima of $\nabla T'$ along the local direction of the gradient vector)
2. Discard centerlines shorter than a certain minimum length
3. Measure layer thicknesses perpendicular to the centerline

This procedure is adopted with the following modifications:

- In step 1, we find the layer centerlines using the gradient of temperature images that are smoothed with twice the local kernel size that is determined by Eq. 1. This increased smoothing is only used for locating the centerlines and does not impact the measured layer thicknesses. If the profiles across the gradient structures were highly asymmetric with respect to the centerline, this increased level of smoothing could artificially shift the locations of the layer centerlines. However, no obvious shifting of the centerlines was observed.
- In step 3, we reduce the uncertainty in determining the layer thicknesses by averaging between 5 and 8 pixels in the local direction of the layer centerlines. This procedure exploits the local anisotropy of the dissipation field. The resulting degradation of spatial resolution is minimal because the averaging is performed along the length of the dissipation layers. Although spatial averaging could introduce artifacts in regions with large curvature, this effect is insignificant with the structure-aligned averaging used in the present analysis.

The half-width at 20% of maximum is measured separately on each side of the layers, and the half-width is doubled to yield the full-width at 20% of maximum, λ_D . If the $|\nabla T'|^2$ profile along layer-normal direction does not monotonically decay to 20% of the local maximum, the layer width is not determined for that point on the layer centerline.

Figure 6, top row, shows the probability density functions (PDF) of the layer widths conditioned on temperature intervals of 200 K for three downstream locations. Each downstream location exhibits a similar temperature-dependent progression of the PDFs. As the temperature increases, the PDFs broaden, and the peaks of the PDFs shift to larger scales. The peak of the PDF increases with axial location. At 600 K, the peak of the PDF shifts from 210 μm to 330 μm . The second row in Fig. 4 shows the same conditional PDFs on a log-log scale. For all temperatures, the PDFs are approximately log-normal distributions. A curve-fit to a log-normal distribution is included for the PDF at 400 K at $x/d = 10$. The deviations at the high temperatures are the result of the lower SNR of the Rayleigh measurements for these temperatures, which can only be partly compensated by the temperature-dependent smoothing scheme.

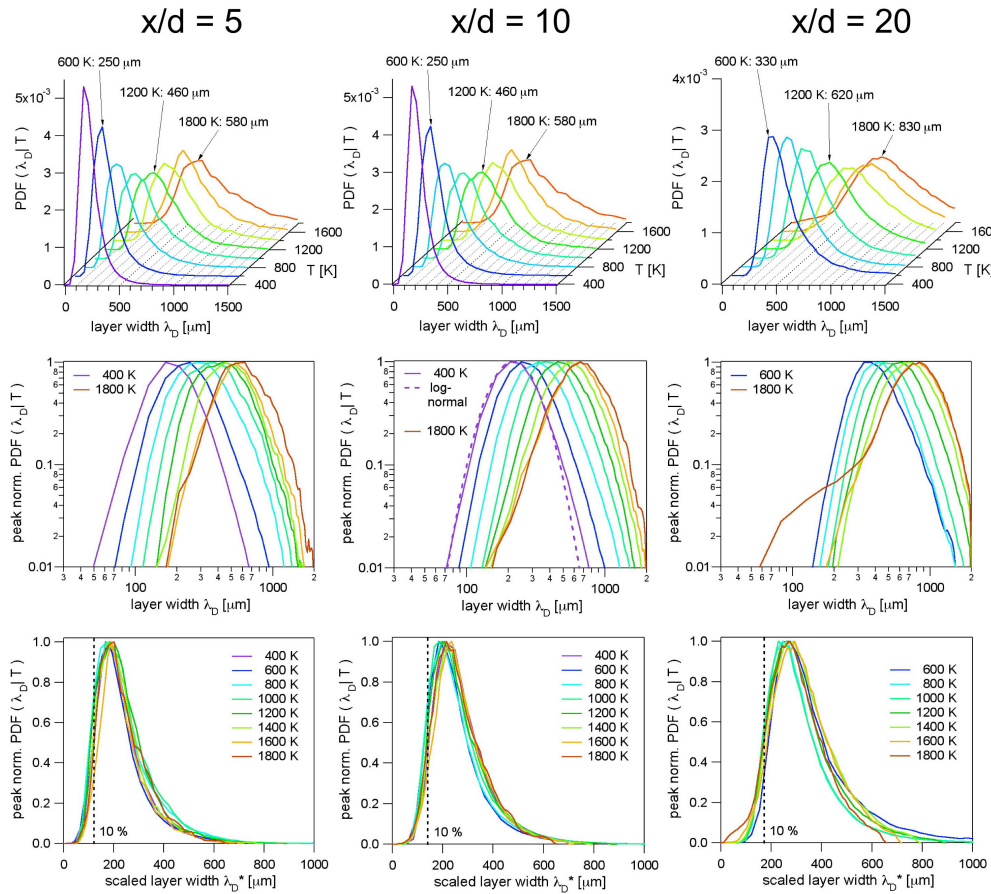


Fig. 6: Probability density functions of $|\nabla T'|^2$ -structure widths conditioned on temperature for three axial locations ($x/d = 5, 10, 20$).

We consider whether the layer thickness PDFs scale with temperature as a simple power law of $(T/T_0)^n$, where $T_0 = 400$ K. The best fit for the power law is determined by plotting each PDF as a function of a scaled width, $\lambda_D^* = \lambda_D(T/T_0)^{-n}$ and evaluating the degree of overlap of the scaled PDFs. The overlap of the PDFs in the third row in Fig. 6 indicates that the PDFs are approximately self-

similar when $n = 0.75$ is used for scaling the layer widths. Although this power dependence is the same as that used in selecting the widths of the filter kernels for adaptive smoothing, the power law scaling of the PDFs is independent of the smoothing process. Indeed, the smoothing parameters were chosen after this power-law scaling became obvious in preliminary analysis because this coincidence of the scaling laws allows for simple, temperature-independent estimation of the errors introduced by the smoothing. Clemens and Wang (2004) showed that in order to measure the 20%-width λ_D of a dissipation structure to within 10% accuracy a resolution corresponding to $\sigma_{\text{gsm}} = \lambda_D/6.1$ is necessary. The vertical dashed lines in the bottom row of Fig. 6. indicate the layer thicknesses above which the error from smoothing is less than 10%. The effects of smoothing introduce less than a 10% error for layer widths that are larger than 150 μm , 175 μm , and 213 μm at $x/d = 5, 10$, and 20, respectively. The value of λ_D at the peak of the PDF is determined with good accuracy for all temperatures and downstream locations.

The spectral analysis in Section 3.1 and the analysis of the layer-width PDFs are complementary approaches to investigating the dissipative length scales. We compare the results of these two approaches by plotting the variation of layer thicknesses and spectral cutoff length scales as a function of radial location. For a characteristic layer width, we use the layer width that corresponds to the logarithmic mean of the PDFs, $\langle \lambda_D \rangle_{\log}$. If the PDF is a log-normal distribution, $\langle \lambda_D \rangle_{\log}$ coincides with the peak of the PDF.

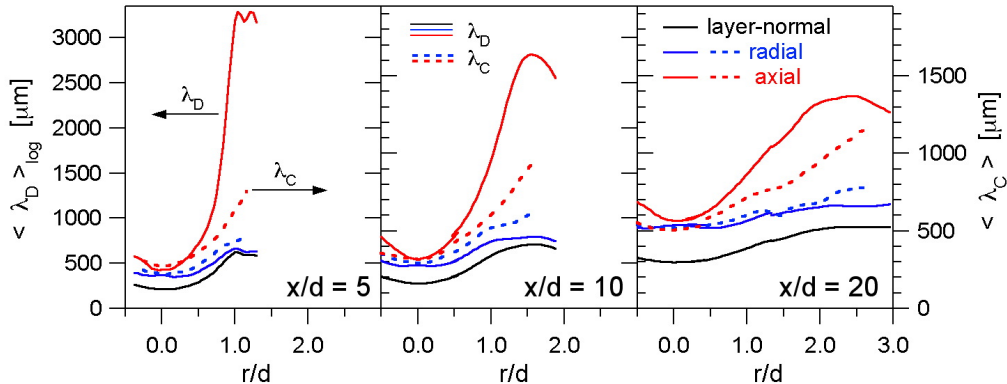


Figure 7. Radial profiles of the spectral cutoff wavelength, λ_C , and the layer thickness, λ_D , at the peak of the layer-thickness PDFs for three axial locations ($x/d = 5, 10, 20$).

Figure 7 compares the radial variation of λ_C and $\langle \lambda_D \rangle_{\log}$ at three downstream locations. Values of λ_C are consistently lower than the corresponding values of $\langle \lambda_D \rangle_{\log}$. The values of λ_C and $\langle \lambda_D \rangle_{\log}$ are plotted on different y-axes and are scaled such that the plots approximately overlap at the jet centerline. The radial and axial projections of λ_D are calculated by $\lambda_{D, \text{rad}} = \lambda_D/|\sin(\beta)|$ and $\lambda_{D, \text{ax}} = \lambda_D/|\cos(\beta)|$, respectively, where β is the local angle between the structure centerline and the radial direction. As shown by Kaiser and Frank (2006), the PDFs of these projected layer-widths deviate from log-normal distributions at large values of λ_D . Therefore, the log-normal means do not necessarily coincide with the peak of the PDFs. In Fig. 7, the radial and axial values of λ_C and $\langle \lambda_D \rangle_{\log}$ monotonically increase with increasing radial position. The best agreement between the radial dependence of λ_C and $\langle \lambda_D \rangle_{\log}$ occurs for the radial projections at $x/d = 20$. For $r/d > 0$, the values of λ_C are systematically larger than the radial projections of $\langle \lambda_D \rangle_{\log}$. In contrast, the values of λ_C from the axial PSDs are systematically smaller than the axial projections of $\langle \lambda_D \rangle_{\log}$ away from the jet centerline. Note that the axial projection of $\langle \lambda_D \rangle_{\log}$ deviates significantly from the

layer-normal values of $\langle \lambda_D \rangle_{log}$ as the preferred orientation of the layers changes with radial location. The maximum length scale of the *PSD* is limited by the dimension of the subregion over which the *PSD* is evaluated. In contrast, the projection of λ_D is not subject to such limitations.

4. Conclusions

High-resolution imaging of laser Rayleigh scattering was used to measure instantaneous thermal dissipation structures in the near field of a turbulent $\text{CH}_4/\text{H}_2/\text{N}_2$ jet flame. The dissipation field was comprised of layered structures with a range of widths. Probability density functions of the layer widths conditioned on temperature were log-normally distributed and exhibited approximate self-similarity when the widths were scaled with temperature according to a power law of $(T/T_0)^{0.75}$. In a spectral analysis of the dissipation fields, fully resolved power spectral densities were measured over three orders of magnitude using an interlacing technique to suppress noise. At $x/d = 20$, the Batchelor scales that were determined from a spectral cutoff wavelength were comparable with estimates based on local Reynolds numbers. At $x/d = 5$ and 10, there was a discrepancy between the two methods for determining the Batchelor scales. The variation of the cutoff wavelengths and the layer-widths were measured as a function of radial position. The radial projection of the layer widths and the radial cutoff wavelength showed similar behavior. The axial projection of the layer widths was significantly larger than the axial cutoff wavelength away from the centerline.

The measurement of length scales and dissipation structures are important for developing accurate combustion models and determining necessary detector resolutions for experimental studies of turbulent flames. The significant variation in length scales with temperature indicates the need for detailed measurements of the dissipation structures to determine the turbulent length scales in the regions where the primary combustion reactions occur. Further highly resolved two-dimensional measurements of dissipation will provide an improved understanding flow-flame interactions in turbulent flames.

Acknowledgements

The authors thank Dr. G. H. Wang for helpful discussions and R. J. Sigurdsson for excellent technical assistance in the laboratory. This research was supported by the U.S. Department of Energy, Office of Basic Energy Sciences, Division of Chemical Sciences, Geosciences, and Biosciences. Sandia National Laboratories is a multiprogram laboratory operated by Sandia Corporation, a Lockheed Martin Company, for the U.S. Department of Energy under contract DE-AC04-94-AL85000.

References

- Barlow RS (2006) Editor: International workshop on measurement and computation of turbulent nonpremixed flames. <http://www.ca.sandia.gov/TNF>
- Bergmann V, Meier W, Wolff D, Stricker D (1998) Application of spontaneous Raman and Rayleigh scattering and 2D LIF for the characterization of a turbulent $\text{CH}_4/\text{H}_2/\text{N}_2$ jet diffusion flame. *Appl Phys B* 66: 489-502
- Buch KA, Dahm WJA (1998). Experimental study of the fine-scale structure of conserved scalar mixing in turbulent shear flows. Part 2. $Sc \approx 1$. *J. Fluid. Mech.* 364: 1-29
- Geyer D (2004), 1D Raman/Rayleigh experiments in a turbulent opposed-jet. Dissertation, Technische Universität Darmstadt (Germany)
- Fielding J, Schaffer AM, Long MB (1998) Three-scalar imaging in turbulent non-premixed flames

of methane. *Proc Combust Inst* 28: 1007-1014

Frank JH, Kaiser SA, Long MB (2002) Reaction-rate, mixture-fraction, and temperature imaging in turbulent methane/air jet flames. *Proc Combust Inst.* 29: 2687-2694

Frank JH, Kaiser SA, Long MB (2005) Multiscalar imaging in partially premixed jet flames with argon dilution. *Combust Flame* 143: 507-523

Frank JH, Lyons KM, Marran DF, Long MB, Stärner SH, Bilger RW (1994) Mixture fraction imaging in turbulent nonpremixed hydrocarbon flames. *Proc Combust Inst* 25: 1159-1166

Kaiser SA, Frank JH (2006) Imaging of dissipative structures in the near field of a turbulent non-premixed jet flame. To be published in *Proc Combust Inst* 31

Karpelis AN, Barlow RS (2002) Measurements of scalar dissipation in a turbulent piloted methane/air jet flame. *Proc Combust Inst* 29: 1929-1936

Karpelis AN, Barlow RS (2005) Measurements of flame orientation and scalar dissipation in turbulent partially premixed methane flames. *Proc Combust Inst* 30: 665-672

Kelman JB, Masri AR, Stärner SH, Bilger RW (1994) Wide-field conserved scalar imaging in turbulent diffusion flames by a Raman and Rayleigh method. *Proc Combust Inst* 25: 1141-1147

Meier W, Barlow RS, Chen YL, Chen JY (2000), Raman/Rayleigh/LIF measurements in a turbulent CH₄/H₂/N₂ jet diffusion flame: experimental techniques and turbulence-chemistry interaction. *Combust Flame* 123: 326-343

Mi J, Nathan GJ (2003) The influence of probe resolution on the measurement of a passive scalar and its derivatives. *Exp Fluids* 34: 687-696

Pope SB (2000) *Turbulent Flows*, Cambridge University Press, New York

Schneider C, Dreizler A, Janicka J, Hassel EP (2003) Flow field measurements of stable and locally extinguishing hydrocarbon-fuelled jet flames. *Combust Flame* 135: 185-190

Smith GP, Golden DM, Frenklach M, Moriarty NW, Eiteneer B, Goldenberg M, Bowman CT, Hanson RK, Song S, Gardiner WC, Lissianski VV, Qin Z (2006) GRI-Mech 3.0. http://www.me.berkeley.edu/gri_mech/

Stärner SH, Bilger, RW, Lyons KM., Frank JH, Long MB (1994) Conserved scalar measurements in turbulent diffusion flames by a Raman and Rayleigh ribbon imaging method. *Combust Flame* 99: 347-354

Su LK, Clemens NT (1999) Planar measurements of the full three-dimensional scalar dissipation rate in gas-phase turbulent flows. *Ex. Fluids.* 27: 507-521

Su LK, Clemens NT (2003) The structure of fine-scale scalar mixing in gas-phase planar turbulent jets. *J Fluid Mech* 488: 1-29

Tsurikov MS, Clemens NT (2002) The structure of dissipative scales in axisymmetric turbulent gas-phase jets. 40th Aerospace Science Meeting, AIAA paper 2002-164

Wang GH, Clemens NT (2004) Effects of imaging system blur on measurements of flow scalars and scalar gradients. *Exp Fluids* 37: 194-205

Wang GH, Clemens NT, Varghese PL (2005a) Two-point, high-repetition-rate Rayleigh thermometry in flames: techniques to correct for apparent dissipation induced by noise. *Appl Optics* 44: 6741-6751

Wang GH, Clemens NT, Varghese PL (2005b) High-repetition rate measurements of temperature and thermal dissipation in a non-premixed turbulent jet flame. *Proc Combust Inst* 30: 691-699

Wang GH, Barlow RS, Clemens NT (2006) Quantification of resolution and noise effects on thermal dissipation measurements in turbulent non-premixed jet flames. To be published in *Proc Combust Inst* 31